

Investigation of the Squeeze Film Dynamics Underneath a Microstructure With Large Oscillation Amplitudes and Inertia Effects

Nadim A. Diab¹

Assistant Professor
Department of Mechanical and
Mechatronics Engineering,
Rafik Hariri University,
Meshref 10-2010, Lebanon
e-mail: diabna@rhu.edu.lb

Issam A. Lakkis

Associate Professor
Department of Mechanical Engineering,
American University of Beirut,
Beirut 11-0236, Lebanon
e-mail: il01@aub.edu.lb

This paper presents direct simulation Monte Carlo (DSMC) numerical investigation of the dynamic behavior of a gas film in a microbeam. The microbeam undergoes large amplitude harmonic motion between its equilibrium position and the fixed substrate underneath. Unlike previous work in literature, the beam undergoes large displacements throughout the film gap thickness and the behavior of the gas film along with its impact on the moving microstructure (force exerted by gas on the beam's front and back faces) is discussed. Since the gas film thickness is of the order of few microns (i.e., $0.01 < Kn < 1$), the rarefied gas exists in the noncontinuum regime and, as such, the DSMC method is used to simulate the fluid behavior. The impact of the squeeze film on the beam is investigated over a range of frequencies and velocity amplitudes, corresponding to ranges of dimensionless flow parameters such as the Reynolds, Strouhal, and Mach numbers on the gas film behavior. Moreover, the behavior of compressibility pressure waves as a function of these dimensionless groups is discussed for different simulation case studies. [DOI: 10.1115/1.4032951]

1 Introduction

With the rapid advancements in microelectromechanical systems (MEMS) technologies in the early 1990s, there emerged a need to better understand the role of squeeze films and their impact on moving microstructures. Applications include radio-frequency (RF) microswitches, micromirrors for optical switching, MEMS accelerometers and gyroscopes, micromotors, and microgas turbines [1–6].

A starting point for researchers is Reynolds lubrication theorem, which was first derived by Blech [7], due to the interest in fluid film behavior in bearings. To better understand the behavior of an MEMS RF switch, many models have been suggested in literature to describe the physical behavior of the gas (usually air) film between the vibrating structure and the underneath fixed substrate. Andrews et al. [8] conducted an experiment to compare the vibrating plate behavior and gas film flow coefficients (spring and damper) with the theoretical results of Ref. [7] and discussed the accuracy of the model at different frequency ranges and plate-structure spacings. Zook et al. [9] experimentally measured the quality factor (i.e., the overall change of energy for molecules hitting the microbeam within one period of oscillation) of a vibrating double-clamped beam microsensor, and their results have been widely used as a benchmark for many models in literature. Guo and Alexeenko [10] used the ellipsoidal statistical Bhatnagar–Gross–Krook model of the equilibrium distribution function in the quasi-steady Boltzmann kinetic model to derive expressions for the gas film damping coefficient and the quality factor. Bao et al. [11] proposed a new model for air damping coefficients in vibratory microsensors operating under low ambient

pressure. Their model uses energy transfer between the moving molecules and the vibrating plate and therefore surpasses Christian's model [12] in two main aspects: the new model is a function of the structure geometry and takes into account the presence of boundaries near the vibrating structure.

The effect of the presence of a fixed boundary near a vibrating substrate was discussed by Newell [13], who studied its effect on the damping coefficient of the squeezed gas film (i.e., quality factor). Hutcherson and Ye [14] modeled the quality factor of a vibrating microbeam and discussed the validity of previous models in literature depending on the boundary conditions assumed (i.e., free oscillating structure as compared to a structure oscillating near a fixed wall). They also relaxed the constant velocity assumption used in Bao's model [11], and the simulated quality factor values for the microbeam resonator were in excellent agreement with the experimental results especially in the free-molecular regime as compared to the transition regime since their MD code was based on the absence of intermolecular forces among the gas molecules. Li and Fang [15] extended the work of Ref. [14] that was limited to parallel plate vibrations to account for rotating plates and bending of microbeams.

Bao et al. [16] also studied the effect of beam tilting by using the nonlinear Reynolds equation and analytically solving for the coefficient of damping torque at nonuniform gap distance. The main restriction of their model is that the damping pressure should be less than the ambient pressure leading to a small squeeze number (the air film viscous force dominant over its spring force). It should be pointed out that the latter assumption is only true for small squeeze number where the operating frequency is significantly less than the mirror first natural frequency leading to an "incompressible" behavior of the gas film as explained by Langlois [17] and Starr [18].

Veijola et al. [19] used analytical models for the gas flow damping coefficient to solve for the capacitance of a perforated plate RF MEMS switch undergoing small amplitude vibrations using circuit analysis. The validity of their model is restricted to

¹Corresponding author.

Contributed by the Tribology Division of ASME for publication in the JOURNAL OF TRIBOLOGY. Manuscript received April 19, 2015; final manuscript received November 23, 2015; published online May 4, 2016. Assoc. Editor: Daniel Nélías.

relatively low switching frequencies (and consequently Reynolds number) and inertia free flows. They modeled the gas flow damping coefficient as sum of contributions of three regions: between substrate and moving plate, through perforated holes, and in the intermediate region between the first two.

Veijola [20] extended the Reynolds squeezed film damping by introducing gas rarefaction and inertia effects and used reduced order modeling (circuit analysis) to solve the resulting improved equations. Gallis and Torczynski [21] modified the Reynolds equation model for squeezed film damping by correcting for the pressure boundary conditions at the beam tips compared to the trivial ambient pressure conditions used before. They used the Navier–Stokes slip-jump and the DSMC methods to determine the new pressure boundary conditions coefficients. Lee et al. [22] extended the work of Veijola [20] and Gallis and Torczynski [21] by accounting for the higher-order bending modes to derive a new squeezed film damping model. Such an extension provided an improved model that yielded better results when compared to experimental data carried by the same authors since it accounts for the bending of the beam structure. Sumali [23] conducted an experiment using a laser Doppler vibrometer to find the gas film damping ratio for a vibrating microparallel plate structure in the free-molecular regime and compared his results to various models in literature [7,8,11,19–21]. Mol et al. [24] argued that Sumali's [23] experimental method is based on modal analysis (i.e., frequency domain) and is therefore complicated since it needs a predefined input driving excitation force. Alternatively, they proposed a time domain electrostatically actuated experiment and validated previous results in literature [11,19,20].

Unlike previous works of literature that are limited to small vibration amplitudes or frequency ranges (up to the vicinity of the cutoff frequency) where the force exerted by the gas on the beam is modeled without detailed investigation of the gas behavior, in this work, the beam is allowed to move at any desired velocity amplitude and frequency (i.e., the distance covered by the vibrating beam could be extended over most of the film gap) and the gas behavior is modeled by the interaction of molecules among themselves and the oscillating microbeam. Therefore, all the thermodynamic properties (density, pressure, temperature, etc.) of the gas along with its velocity can be found at any position within the gap film. This way, a complete analysis of the gas behavior along with its effect on the vibrating beam can be performed which sheds more light on the underlying dynamics of the interaction between the moving structure and the surrounding gas.

2 Methodology

The objective of this work is to develop the authors' previous work [25,26] by using the DSMC method [27–29] to model the behavior of the gas film between a microplate (width \gg length)

undergoing large amplitude oscillations ($V_{\text{beam}} = V_a \sin(2\pi ft)$) and the fixed substrate underneath (Fig. 1). Figure 2 shows the two-dimensional computational domain as modeled in the DSMC code defined by the rectangle ABCD due to symmetry about the beam's centerline ZZ' (Fig. 1). AB is defined as a symmetry plane undergoing specular reflection whereas the substrate BC along with the beam faces (EF, FG, and GH) are all modeled as diffusive walls at ambient temperature. The domain is divided into simulation and reservoir cells where each cell is divided into four sub-cells. The enclosed region ADCC'IA'A contains the reservoir cells that are modeled to impose the desired boundary conditions of ambient temperature and pressure.

3 Dimensionless Groups

To better understand the behavior of the microbeam under different conditions, dimensionless groups are defined based on the physical parameters of interest. To start with the oscillating beam, the parameters involved are the beam width (b), beam velocity with amplitude (V_a) and direction normal to the fixed substrate, and the vibrating frequency (f). For the gas medium surrounding the microbeam, the physical parameters involved are the gas molecular diameter (M_d), the gas molecular mass (M_m), the gas-specific heat ratio (γ), the gas density (ρ), the gas mean free path

$$\lambda = \frac{M_m}{\sqrt{2\pi\rho M_d^2}} \quad (1)$$

the speed of sound in the gas medium

$$a = \sqrt{\frac{\gamma kT}{M_m}} \quad (2)$$

where k is the Boltzmann constant, and T is the temperature, and the gas dynamic viscosity

$$\mu = \frac{M_m}{3\sqrt{2}\pi M_d^2} \sqrt{\frac{8kT}{\pi M_m}} \quad (3)$$

Since viscosity is a continuum concept and the gas flow in the gap film is in the noncontinuum regime ($\text{Kn} > 0.01$), the effective viscosity (μ_{eff}) is used according to Veijola's model [30]

$$\mu_{\text{eff}} = \frac{\mu}{1 + 9.638 \left(\frac{\lambda}{h_0} \right)^{1.159}} \quad (4)$$

This correction of the viscosity accounts for the boundary slip flow due to gas rarefaction near the wall.

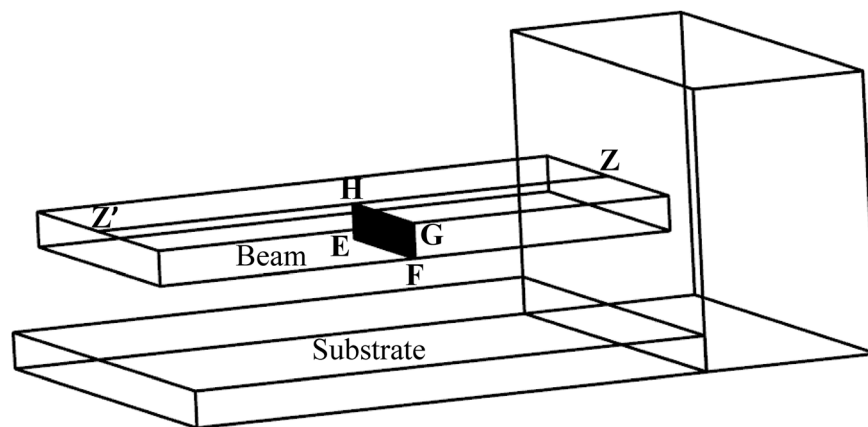


Fig. 1 Three-dimensional schematic of the microbeam

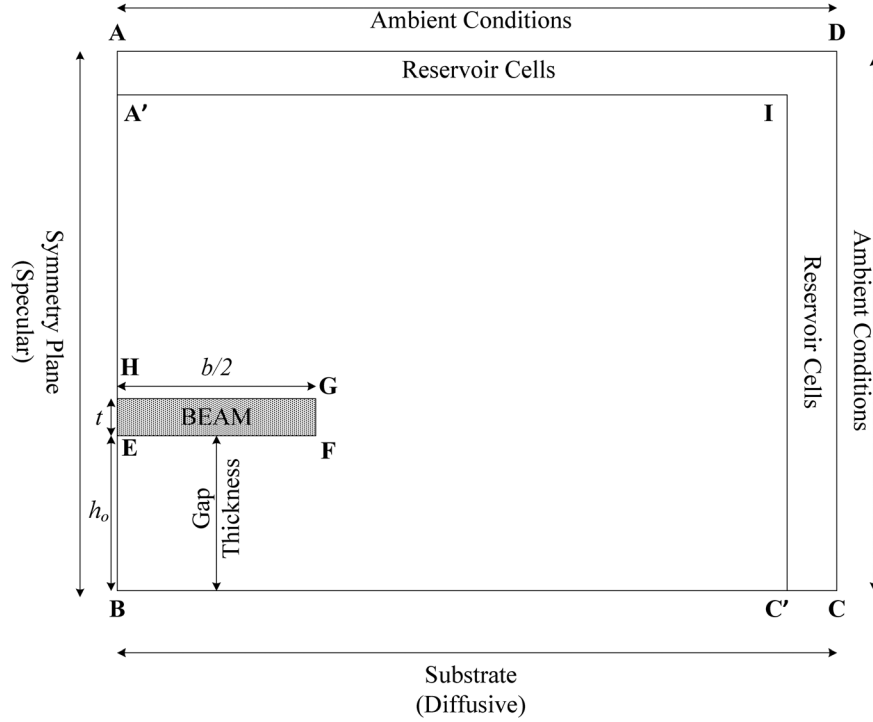


Fig. 2 Two-dimensional simulation domain

For the simulation domain, the gap film thickness (h_0) and the beam width (b) are the main physical parameters influencing the gas flow behavior.

A set of dimensionless groups that capture all the physical parameters mentioned previously are formed. The Knudsen number, which determines the degree of rarefaction and the flow regime (continuum versus noncontinuum), is the ratio of the molecular mean free path to the characteristic flow length scale

$$\text{Kn} = \frac{\lambda}{h_0} \quad (5)$$

The Reynolds number is defined as the ratio of the momentum convection term (inertia forces) to the momentum diffusion term (viscous forces)

$$\text{Re} = \frac{V_a h_0}{\nu} = \frac{\tau_{\text{diff}}}{\tau_{\text{conv}}} \quad (6)$$

where the film gap thickness (h_0) is the characteristic length scale, the beam's velocity amplitude (V_a) is the characteristic speed scale, $\nu = \mu_{\text{eff}}/\rho$ is the kinematic viscosity, and $\tau_{\text{conv}} = h_0/V_a$ and $\tau_{\text{diff}} = h_0^2/\nu$ are the convection and diffusion time scales, respectively. The microbeam undergoes harmonic oscillatory motion (unsteady), and the Strouhal number (St) is introduced to nondimensionalize the unsteady component of the inertia term. The Strouhal number is the ratio of inertial forces due to flow oscillations (i.e., local acceleration due to change of velocity with time where the oscillatory time scale is given by $\tau_{\text{osc}} = 1/f$) to the convection term (i.e., acceleration due to spatial change of velocity)

$$\text{St} = \frac{\tau_{\text{conv}}}{\tau_{\text{osc}}} = \frac{f h_0}{V_a} = \frac{h_0}{2\pi\delta} \quad (7)$$

where δ is the maximum displacement amplitude of the vibrating beam, given by $\delta = V_a/2\pi f$. Note that, alternatively, Strouhal number measures the ratio of the gap thickness to the maximum distance traversed by the vibrating beam. Another dimensionless

group of interest is the Mach number (Ma), the ratio of the characteristic gas flow speed to the speed of sound in the gas medium

$$\text{Ma} = \frac{V_a}{a} \quad (8)$$

where a is the speed of sound, is expressed as $a = \sqrt{\gamma kT/M_m}$. For an ideal gas, Ma, Re, and Kn are related according to

$$\text{Kn} = \sqrt{\frac{\pi\gamma}{2}} \frac{\text{Ma}}{\text{Re}} \quad (9)$$

Finally, the beam width (b) is normalized according to the characteristic length scale (h_0) as

$$b^* = \frac{b}{h_0} \quad (10)$$

Note that the squeeze film number, which measures the relative importance of viscous forces to spring forces, may be expressed as

$$\sigma_d = \frac{24\pi\mu b^2 f}{h_0^2 P_0} = 24\pi\gamma \text{St} \frac{\text{Ma}^2 (b^*)^2}{\text{Re}} = \pi^2 \frac{f}{f_c} \quad (11)$$

where f_c is the cutoff frequency defined as

$$f_c = \frac{\pi h_0^2 P_0}{24\mu b^2} \quad (12)$$

In what follows, this cutoff frequency will be referred to as ideal cutoff frequency as it is valid for the set of restrictions and assumptions used to formulate the Reynolds equation [7]:

- (1) The gap h_0 is much smaller than the microplate dimensions,
- (2) microplate is oscillating at low Re number and hence inertia effects are neglected,
- (3) trivial boundary conditions at microplate edges, and
- (4) no pressure gradient in the direction normal to microplate motion.

Table 1 List of dimensionless groups for the various simulated case studies

	Kn	Re ($\tau_{\text{diff}}/\tau_{\text{con}}$)	St ($\tau_{\text{con}}/\tau_{\text{osc}}$)	Ma	St·Ma ² /Re ($\sigma_d/(24\pi\gamma b^*{}^2)$)	Re·St ($\tau_{\text{diff}}/\tau_{\text{osc}}$)	Ma·Kn ($\tau_{\text{coll}}/\tau_{\text{con}}$)	Ma·Kn·St ($\tau_{\text{coll}}/\tau_{\text{osc}}$)	Ma·Kn/Re ($\tau_{\text{coll}}/\tau_{\text{diff}}$)
Case 1: Varying V_a ($f = 1$ GHz, gas: air)									
V_a (m/s)									
20	0.068	1.889	50	0.058	0.09	94.43	0.004	0.198	0.002
100	0.068	9.443	10	0.292	0.09	94.43	0.02	0.198	0.002
200	0.068	18.886	5	0.583	0.09	94.43	0.04	0.198	0.002
400	0.068	37.772	3	1.166	0.09	94.43	0.079	0.198	0.002
Case 2: Varying f ($V_a = 90$ m/s, gas: air)									
f (MHz)									
100	0.068	8.499	1.111	0.262	0.009	9.443	0.018	0.02	0.002
500	0.068	8.499	5.556	0.262	0.045	47.215	0.018	0.099	0.002
1000	0.068	8.499	11.111	0.262	0.09	94.43	0.018	0.198	0.002

It will be shown later that such an ideal cutoff frequency will differ from the cutoff frequency for the simulated cases where all of the above assumptions are no longer valid.

Note that a scales as the most probable speed, the ratios of the collision time scale to convection, diffusion, and oscillation time scales, expressed in terms of dimensionless quantities, are, respectively,

$$\frac{\tau_{\text{coll}}}{\tau_{\text{conv}}} \approx \frac{\lambda/a}{h_0/V_a} = (\text{Ma})(\text{Kn}) \quad (13)$$

$$\frac{\tau_{\text{coll}}}{\tau_{\text{diff}}} = \frac{\tau_{\text{coll}}}{\tau_{\text{conv}}} \frac{\tau_{\text{conv}}}{\tau_{\text{diff}}} \approx \frac{(\text{Ma})(\text{Kn})}{\text{Re}} \quad (14)$$

$$\frac{\tau_{\text{coll}}}{\tau_{\text{osc}}} = \frac{\tau_{\text{coll}}}{\tau_{\text{conv}}} \frac{\tau_{\text{conv}}}{\tau_{\text{osc}}} \approx (\text{Ma})(\text{Kn})(\text{St}) \quad (15)$$

4 Results and Discussion

Hereafter, simulations are performed that cover a range of values of the various dimensionless groups as listed in Table 1. It is worth noting that these dimensionless groups were formed by time-scale analysis presented before and by the authors' analytical work in Ref. [25]. All the results are presented in terms of normalized quantities after simulating the flow over a large number of periods (i.e., quasi-steady state); the flow velocity is normalized with respect to the beam's velocity amplitude (V_a), pressure is normalized with respect to the relevant gas atmospheric pressure at 20 °C, density is normalized with respect to relevant gas density at 20 °C, force is normalized with respect to the product of the atmospheric pressure and the microbeam's area, and time is normalized (τ_{norm}) with respect to the beam's oscillation period (T). Table 2 summarizes the geometrical parameters used and the ambient gas medium (air) physical conditions. The relation between the gas flow behavior and the force imparted on the beam is interpreted in terms of the relative importance of diffusion and inertia, where the latter is the superposition of an unsteady term and a convective term.

In what follows, all results correspond to quasi-steady conditions at times longer than the transients time that arise from the

initial conditions. The results are presented in terms of the flow speed in the direction normal to the beam at the symmetry plane BA (Fig. 2) near the oscillating beam as a function of time and the force acting on the beam as a function of time.

4.1 Effect of Reynolds Number. The first set of simulations investigates the relative impact of convection and diffusion momentum on the gas dynamics in the vicinity of the microbeam. This is studied by varying the beam speed amplitude (20–400 m/s) while keeping a constant 1 GHz beam oscillation frequency. The corresponding ranges of Reynolds and Mach numbers are $1.9 \leq \text{Re} \leq 38$ and $0.058 \leq \text{Ma} \leq 1.166$, while Re St remains constant. The dynamic behavior of the gas velocity near the beam at the symmetry plane, shown in Fig. 3, shows that the gas velocity amplitude approaches the vibrating beam velocity amplitude as Reynolds number increases. This is expected since larger Reynolds number implies an increasing role of the convective component of the inertia term with respect to diffusion. In terms of molecular behavior, as the beam velocity increases the inertia transfer to molecules (i.e., momentum of convection) becomes more dominant, and therefore, the gas behavior gets closer to the beam motion governed by τ_{osc} . So as the beam starts moving away from the substrate, how quickly it responds to the beam motion and follows it depends on both the beam speed and the Reynolds number of the flow. For small V_a , the beam slow motion allows the flow (with smaller Re) to take longer time to respond to the beam change in motion direction, whereas for larger V_a , the fast moving beam (away from the substrate) forces the flow to respond more quickly. In summary, the cases with larger Re have asymmetric response of the flow velocity in its vicinity due to strong inertia effects, whereas the response is close to harmonic for the small Re case. This same effect explains why the flow reverses its direction during the first half period (rise time) much faster than it does in the second half period (drop time) for flows with high flow inertia (i.e., Re).

The gas dynamics discussed before is reflected on the forces at both sides of the microbeam. In terms of the beam's front face force (solid line), the same inertia effect explained before imposes a high force amplitude during the first half period (collision of a relatively high number of molecules moving away from substrate due to inertia effects with the beam moving toward the substrate) as compared to the second half period (molecules keep moving toward the substrate due to inertia effects while the beam is moving away from the substrate). The same phenomena can be observed on the beam's back face force (dashed line) with the difference that during the second half period, the flow propagates away from the beam toward the ambient boundary rather than the substrate. Figure 4 also shows that the force amplitude on the beam's front face (facing the substrate) during the first half of the period (as the beam moves toward the substrate) is larger than the force amplitude on the beam's back face during the second half of the period (as the beam moves away from the substrate). This is expected due to the squeeze film effect; the back face is open to the atmosphere whereas the front face senses the higher

Table 2 Microbeam geometry and gas flow conditions

Physical property	Symbol	Value
Beam width	b	2 μm
Beam thickness	t	0.1 μm
Initial gap height	h_o	1 μm
Excitation frequency	f	100 MHz to 1 GHz
Velocity amplitude	V_a	20–1000 m/s
Ambient temperature	T_o	293 K
Ambient pressure (air)	P_o	101.1 KPa

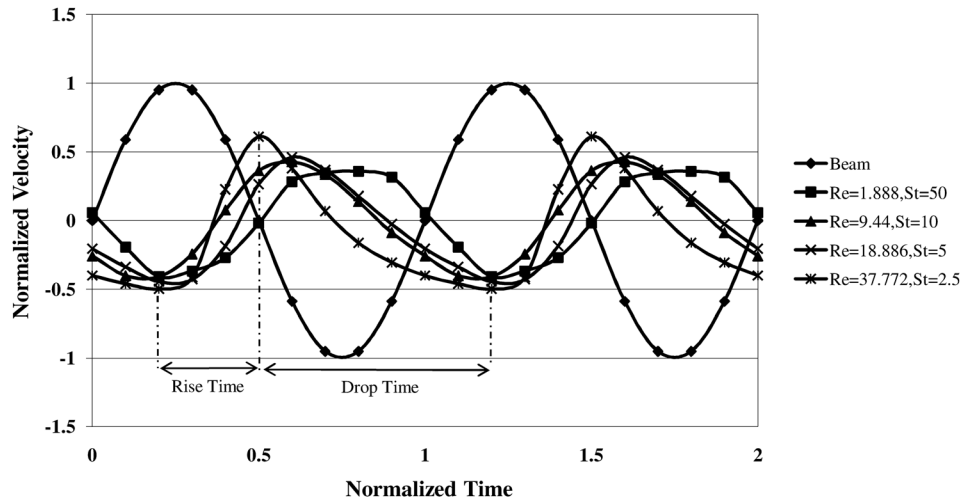


Fig. 3 Flow velocity of gas film at first cell next to the beam within the gas film gap

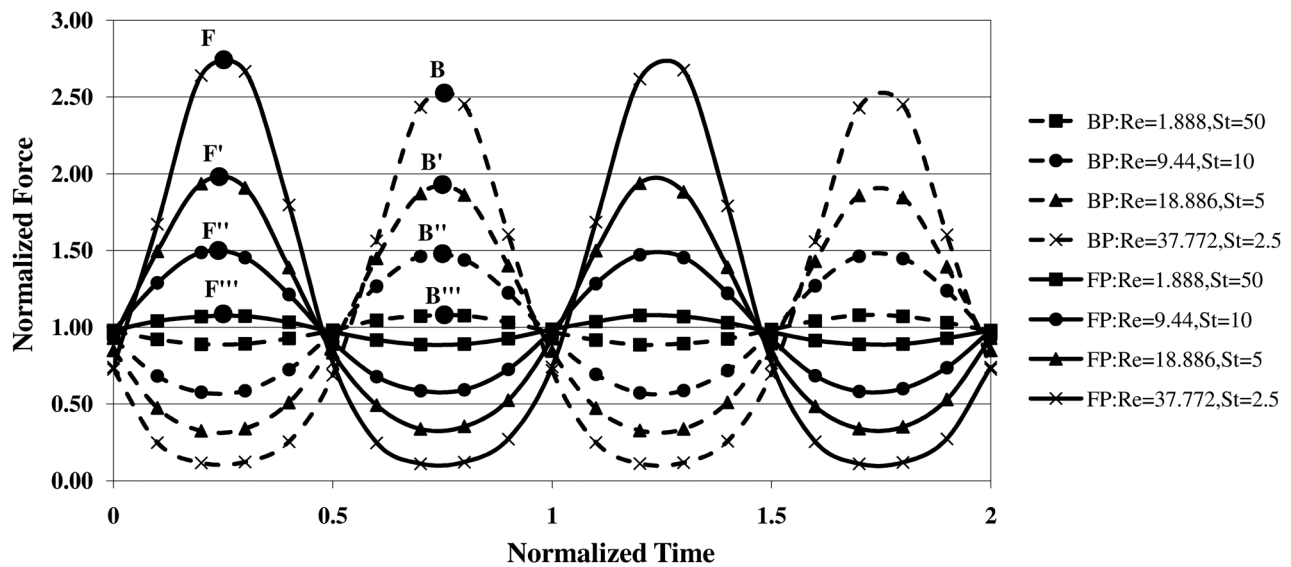


Fig. 4 Forces at beam's front and back faces

pressure of the squeeze film in the gap. The amplitude of the net force on the beam (difference between force on front face and force on back face) increases for larger values of Re . As can be seen from Fig. 4, as Re increases, the beam's front face force amplitude increases as seen by points $F, F', F'',$ and F''' . The same trend is observed at the beam's back face force (dashed line) amplitude represented by points $B, B', B'',$ and B''' . This behavior is expected since convection plays a bigger role as Re increases, which is associated with larger momentum transfer to the beam due to collisions with fluid molecules, thus exerting a larger force on the vibrating beam.

4.2 Effect of Strouhal Number. In the second set of simulations, the beam's speed amplitude is fixed at 90 m/s and the frequency is varied: 100 MHz, 500 MHz, and 1 GHz. Figures 5 and 6 show, respectively, time evolution of gas velocity at the first cell next to the beam within the film gap and the forces acting on the beam back and front beam face forces. Note that Reynolds number remains the same, the relative contribution of diffusion with respect to convection does not change. However as the frequency of the plate motion decreases, the product of Re and St decreases, indicating a smaller role of the unsteady component of

inertia (compared to diffusion) which brings the flow motion (phase and magnitude) closer to the beam motion, as shown in Fig. 5.

The forces exerted by the gas on the oscillating beam front and back faces are shown in Fig. 6. It is observed that the force amplitude is highest for the beam oscillating with the highest frequency (point F). Interestingly, for the case of beam oscillating at 100 MHz, the force on the beam front face experiences a huge drop when compared to the high frequency cases. To better understand this behavior, density contours are plotted at two different time frames within the period; the first (Fig. 7) refers to the normalized time ($\tau_{norm} = 0.3$) at which the beam is moving with maximum velocity toward the fixed substrate while the second (Fig. 8) refers to the normalized time ($\tau_{norm} = 0.8$) at which the beam is moving with maximum velocity away from the fixed substrate. In the first plot (Fig. 7), the high-density region is just next to the beam and decreases as one moves toward the substrate. For small beam oscillation frequencies, $Re St$ is smaller indicating that diffusion plays a larger role when compared to that of the flow inertia. This means that molecules have "enough" time to diffuse from the high-density region next to the beam to the surrounding low-density regions. This effect plays a major role in relaxing the pressure at the beam's front face as compared to the

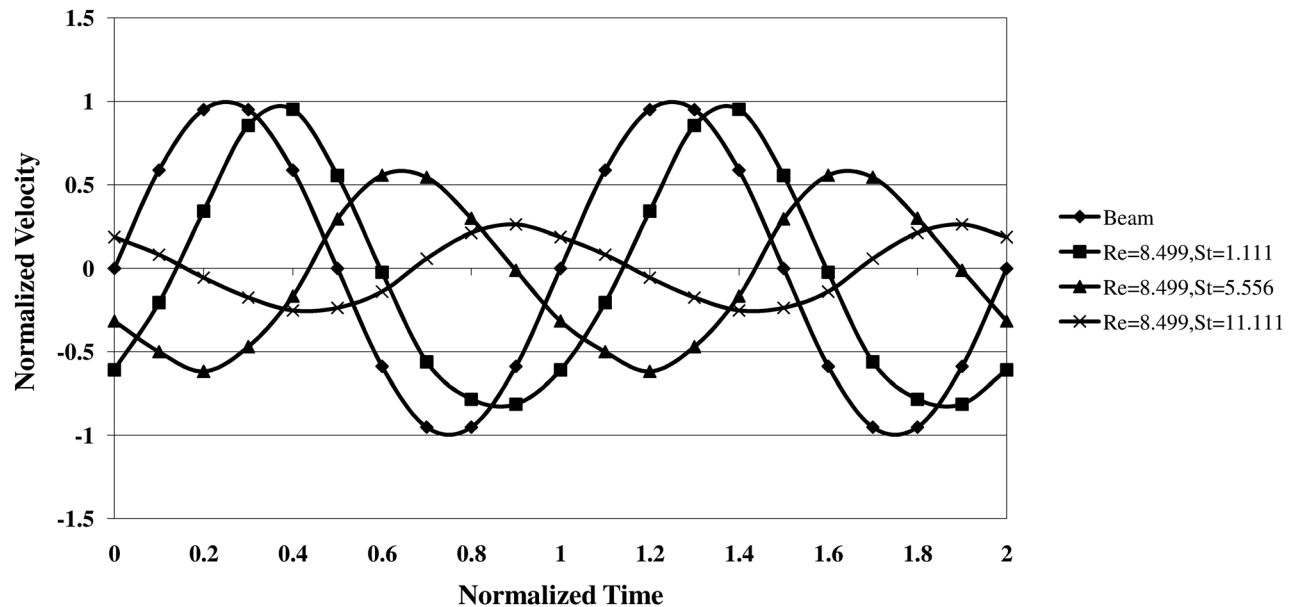


Fig. 5 Flow velocity of gas film at first cell next to the beam within the gas film gap

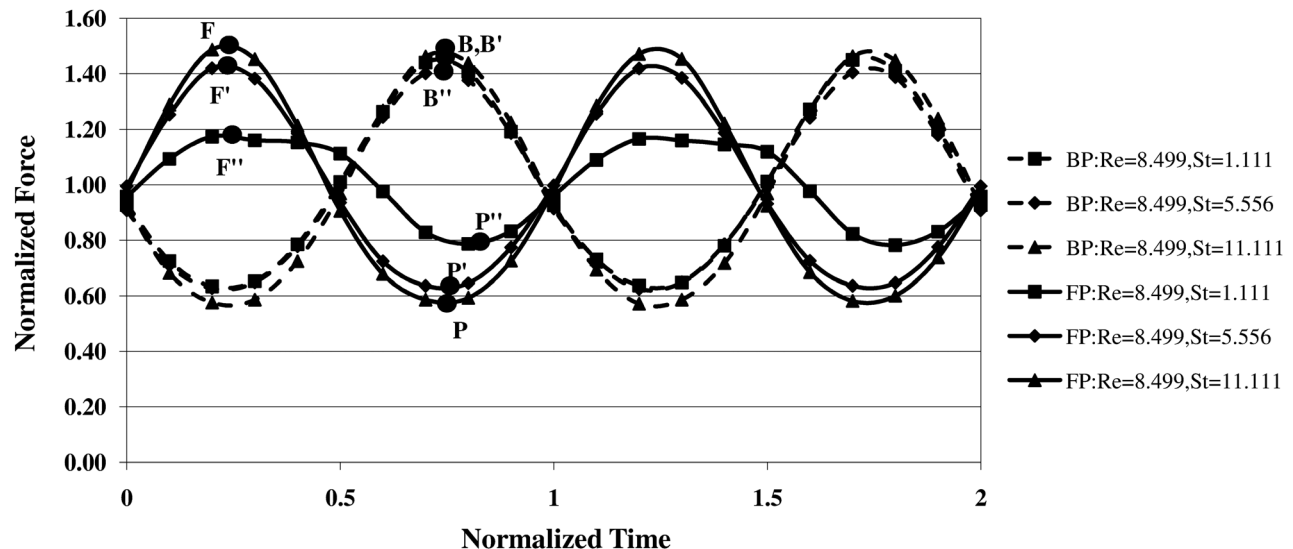


Fig. 6 Forces at beam's front and back faces

cases of 500 MHz and 1 GHz (points F'' , F' , and F , respectively, in Fig. 6) where molecules do not have enough time to diffuse (i.e., gas entrapment that corresponds to high squeeze number). When the beam is moving away from the substrate, (Fig. 8), similar argument can be made: the density just next to the beam is low and increases as we move further toward the substrate. Having a high diffusion rate, molecules have enough time to diffuse from the high-density region away from the beam to the low-density region just next to the beam. This results in higher pressure at the beam's front face as compared to the 500 MHz and 1 GHz cases (points P'' , P' , and P , respectively, in Fig. 6). As the beam stops and reverses its oscillating direction (i.e., $\tau_{\text{norm}} = 0.5$), the relatively high diffusion rate of the 100 MHz beam acts against inertia (both Re and $Re St$ are relatively small) and tends to "fill in" the low-density region just next to the beam surface and therefore keeps a higher force (i.e., phase shift) on the beam as compared to the other two high frequency (low diffusion) cases where the force is very close to that exerted by the atmospheric pressure.

Note that at the beam's back face, the force is almost constant (points B'' , B' , and B in Fig. 6) due to the fact that the back plate

face is open to the atmosphere, and therefore, no "gas entrapment" effect is experienced by the flow.

4.3 Compressibility Effects. Since the microbeam operates in a gas medium (usually air), compressibility effects are expected to play a significant role in the flow dynamics and consequently on the force acting on the microbeam. In the absence of body forces (which applies in microflows), a fluid behaves as incompressible [31] when $Ma^2 \ll 1$, $Ma^2 St \ll 1$, $Ma^2 St^2 \ll 1$, and $Ma^2/Re \sim Kn Ma \ll 1$. In what follows, compressibility effects are discussed for a microbeam oscillating in air with the same geometry as that considered earlier (Table 2) with a gap thickness $h_0 = 0.5 \mu\text{m}$. It follows from Eqs. (7) and (8) that, for $Ma^2/Re \ll 1$, the beam's velocity amplitude (V_a) and oscillating frequency (f) are the two physical parameters that predominantly affect the compressibility in the gas film.

Table 3 lists physical and dimensional parameters for the cases investigated. In the first set of simulations, Ma^2 is varied from 0.35 to 5.54 while $Ma^2 St^2$ and the beam oscillating frequency are

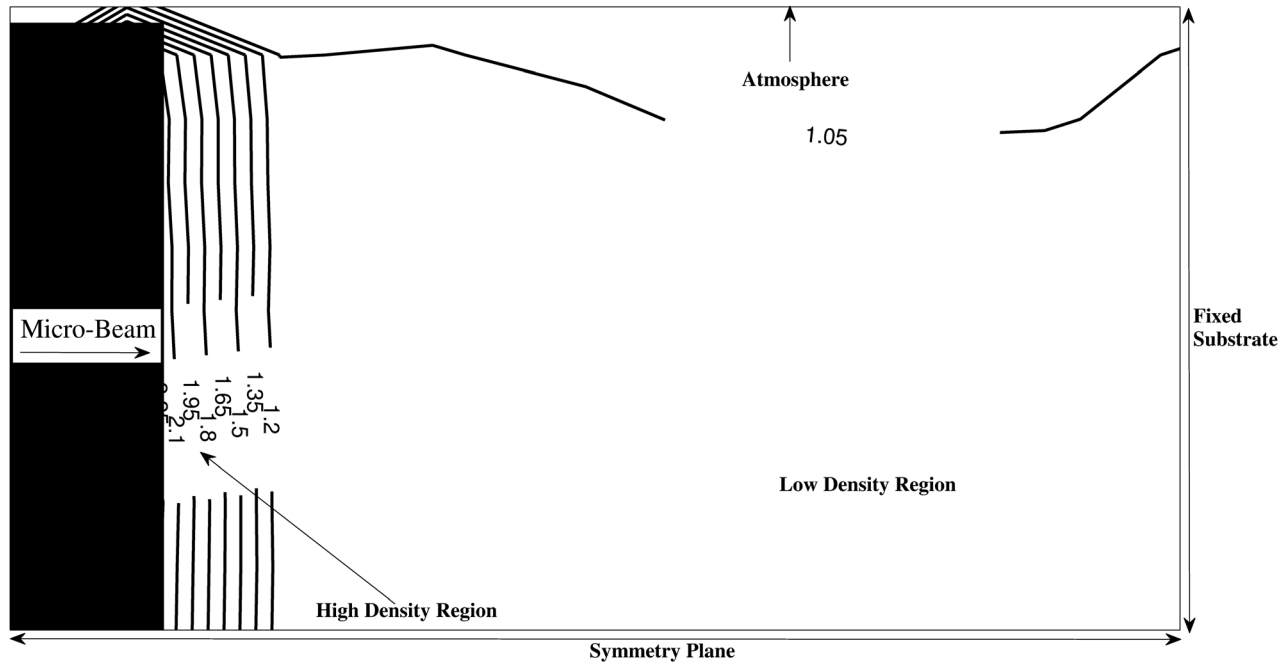


Fig. 7 Density contours within the film gap thickness at $\tau_{norm} = 0.3$

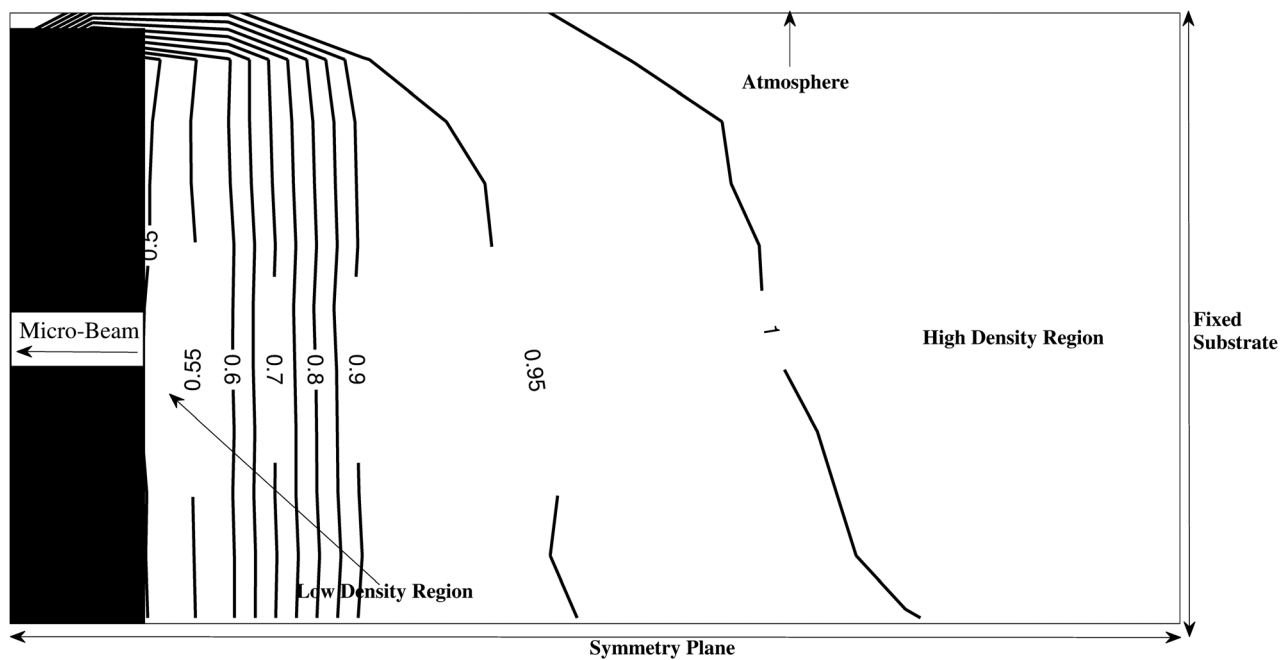


Fig. 8 Density contours within the film gap thickness at $\tau_{norm} = 0.8$

kept constant with respective values of 8.65 and 1 GHz. In the second set, Ma^2 is kept fixed at 0.07 (for a constant velocity amplitude of 90 m/s) while $Ma^2 St^2$ is varied from 0.09 to 8.65, and in the third set, Ma^2 is varied from 0.21 to 3.0 while St is kept constant at a value of 0.64.

When the beam oscillates toward the fixed substrate (i.e., during the first half period, $\tau < 0.5$), it forms a high-pressure wave in the “inside region” and a low-pressure wave in the “outside region,” where the inside region and the outside region refer, respectively, to the squeeze film region between the beam and substrate and the region between the beam and the atmosphere. The opposite happens when the beam reverses its oscillation direction. The pressure waves initiated by the beam oscillatory

motion interact with the pressure waves in the flow field (formed at previous time steps) that could be traveling in or opposite to the beam direction of motion. This interaction could be constructive if both waves are expansion or compression waves and destructive otherwise. The average speed of the pressure waves (V_{pw}/V_a) in the flow field, for $Ma^2/Re \ll 1$, depends on both Ma and St . Figures 9(a) and 9(b) show the time evolution of the pressure and temperature at the plane of symmetry (BA in Fig. 2) over a full period for two cases: case (a) is low compressibility case with $V_a = 90$ m/s and $f = 100$ MHz (set 2, $Ma^2 = 0.07$, $Ma^2 St^2 = 0.087$), while case (b) is a high compressibility case with $V_a = 800$ m/s, $f = 1$ GHz (set 1, $Ma^2 = 5.536$, $Ma^2 St^2 = 8.651$). The pressure and temperature distributions shown in Figs. 9(a)

Table 3 List of values for Ma^2 and Ma^2St^2 for the compressibility simulation case studies

		St	Ma^2	Ma^2St^2	Ma^2/Re
Set 1					
V_a (m/s)	f (MHz)				
200	1000	5	0.346	8.651	0.018
400	1000	2.5	1.384	8.651	0.037
600	1000	1.667	3.114	8.651	0.055
800	1000	1.25	5.536	8.651	0.073
Set 2					
V_a (m/s)	f (MHz)				
90	100	1.111	0.07	0.087	0.008
90	500	5.556	0.07	2.163	0.008
90	1000	11.111	0.07	8.651	0.008
Set 3					
V_a (m/s)	f (MHz)				
50π	100	0.64	0.213	0.087	0.014
100π	200	0.64	0.854	0.346	0.029
125π	250	0.64	1.334	0.541	0.036
151.51π	303	0.64	1.960	0.794	0.044
187.5π	375	0.64	3.002	1.216	0.054

and 9(b) are presented along the plane of symmetry that spans both the “inside” and “outside” flow regions.

Since both Ma^2 and Ma^2St^2 are significantly larger in case (b) when compared to case (a), we expect compressibility effects to be stronger in case (b). This is manifested in terms of larger variations in pressure and temperature as observed in Fig. 9(b) compared to those observed in Fig. 9(a). Figure 9(a) shows that the pressure wave in the outside region of the beam is characterized by a periodic spatial variation with a mean equal to the far-field pressure and an amplitude that decays away from the beam. The spatial rate of decay of the pressure wave amplitude is expected to be caused by viscous dissipation with larger decay rates for smaller values of Re . The speed at which the wave is traveling, which is estimated by dividing the distance a peak travels over one period of beam oscillation by the beam oscillation period, is close to a , the local speed of sound in the medium. In the inside region, however, it can be seen that the pressure wave undergoes a single period per beam oscillation period, indicating that, unlike in the outside region, the pressure wave travels at the average plate speed in the inside region. Figure 10(a) shows the time evolution of the density (normalized by atmospheric density) field over one period of beam oscillation for case (a). By comparing Figs. 9(a) and 10(a), it can be seen that regions of low and high pressure coincide, respectively, with regions of low- and high-density. Strongest compression is observed inside the gap at $\tau \sim 0.4$, while strongest rarefaction is observed at $\tau \sim 0.9$, which indicates that gas compressibility in the gap is almost in phase with the beam motion. The corresponding temperature profiles, plotted in Fig. 9(a), show that the spatial temperature distribution generally follows the pressure, but with smaller variations due to thermal diffusion that tends to bring the temperature distribution toward its far-field (atmospheric) value. Note that the normalized temperature of both the beam and the substrate is unity, the average temperature inside the gap is above unity for the compression half period ($0 < \tau < 0.5$) and less than unity for the expansion half period ($0.5 < \tau < 1$). For the high compressibility case, case (b), one can notice from the time evolution of the pressure distribution along the symmetry plane over a full beam oscillation period, shown in Fig. 9(b), that there exists a zone in the outside region ($2\mu\text{m} < x < 5.35\mu\text{m}$) where the pressure maintains a persistent distribution irrespective of the beam motion. The periodic beam motion at high speed (800 m/s) and high frequency (1 GHz) seems to affect only the immediate neighborhood of the beam since the beam is oscillating so fast which generates alternate compression and expansion waves that “kill” each other since they do not have enough time to propagate away from the beam and “survive.” Figure 10(b) shows the time evolution of the density (normalized by atmospheric density) field over one period of

beam oscillation for case (b). The fact that the beam is oscillating at a very high-speed at a very high frequency creates a low-density region in its vicinity. In other words, there is not enough time for the molecules to fill in the low-density region created by the beam’s oscillation, sweeping out all molecules in its way. Molecules that hit the beam are reflected to a distance relatively far from the beam creating two high-density regions on both sides of the beam, one at the substrate in the inside region and another in the outside region where $2\mu\text{m} < x < 5.35\mu\text{m}$. If the beam was moving at a slower speed, as in Fig. 10(a) for case (a), molecules would not be reflected far from it, and therefore, they can more quickly fill in the low-density region. Similarly, if the beam had a high speed but lower frequency, then the molecules are still reflected away from the beam but now they have more time to fill in the low-density region because of the relatively low oscillating frequency.

In support of the argument that the high-speed and high frequency of the beam lead to the observed behavior of case (b), reducing the speed from 800 m/s to 200 m/s, while keeping the frequency at 1 GHz (set 1 in Table 3), shows a persistent high-pressure zone in the outside region neighboring the beam for beam velocities larger than 400 m/s, as seen in Fig. 11. Figure 11 shows the pressure variation along the beam’s plane of symmetry (BA in Fig. 2) starting from the fixed substrate to the end of the simulation domain (i.e., ambient atmospheric conditions) at $\tau_{\text{norm}} = 0.9$. The figure also shows that as Ma^2 increases, the amplitude of the high-pressure wave on both sides of the beam increases as seen by the two set of points ($H, H', H'',$ and H''') and ($I, I', I'',$ and I'''). Similarly, the amplitude of the low-pressure waves increases with increasing Ma^2 as illustrated by the two set of points ($L, L', L'',$ and L''') and ($O, O', O'',$ and O'''). This observation is in accordance with the fact that compressibility effects become much more significant with higher Mach numbers.

Pressure distributions along the beam’s plane of symmetry (BA in Fig. 2) at $\tau = 0.9$ are shown in Fig. 12 for the low Mach number cases of set 2. Note that in the outside region, the low-pressure wave is initiated during the first half period of motion and the high-pressure wave is initiated during the second half period, it is expected that the distance between the peaks (wavelength) increases as the period increases. This is confirmed in Fig. 12 where the distance d between the alternative cusps increases as the frequency decreases (i.e., $d_{100\text{MHz}} > d_{500\text{MHz}} > d_{1\text{GHz}}$). For all the cases of set 2, and for which $Ma \ll 1$, the speed of the pressure waves is approximately the speed of sound. This behavior, in contrast to that of the high frequency cases of set 1, is attributed to the relatively low frequency of the beam. For the low frequency beam (100 MHz), once a compression wave is formed, the beam takes much more time to oscillate back as compared to that of high frequency ($f = 1\text{GHz}$) and this allows the wave to propagate for longer distances and “escape” the destructive effect of the low-pressure wave created by the beam. In the inside region, it may be observed from Fig. 12 that, toward the end of the beam oscillation period ($\tau = 0.9$), the compressibility pressure waves for beam oscillation frequencies of 1 GHz and 500 MHz (points I' and I'') are still moving toward the substrate as compared to the 100 MHz case (point I). This is because low beam oscillation frequency allows enough time for the gas to follow the beam motion. Figure 12 also shows that the pressure wave peaks amplitude (see points $H_T, H'_T,$ and H''_T) decreases as St increases due to the kill and survive effect explained before. The compressibility pressure wave of the 100 MHz “survived” due to the relatively low microbeam’s oscillating frequency and consequently has a higher peak than those with high frequencies although the values of Ma^2 and Ma^2St^2 are smaller.

To shed more light on this behavior, an additional set of simulations (set 3 of Table 3) is presented where Ma^2 is varied from 0.21 to 3 for fixed $St = 0.6366$ (Ma^2St^2 varies from 0.09 to 1.22). Figure 13 shows that the pressure wave peak amplitude in the inside region increases as Ma^2 increases from 0.213 to 1.334

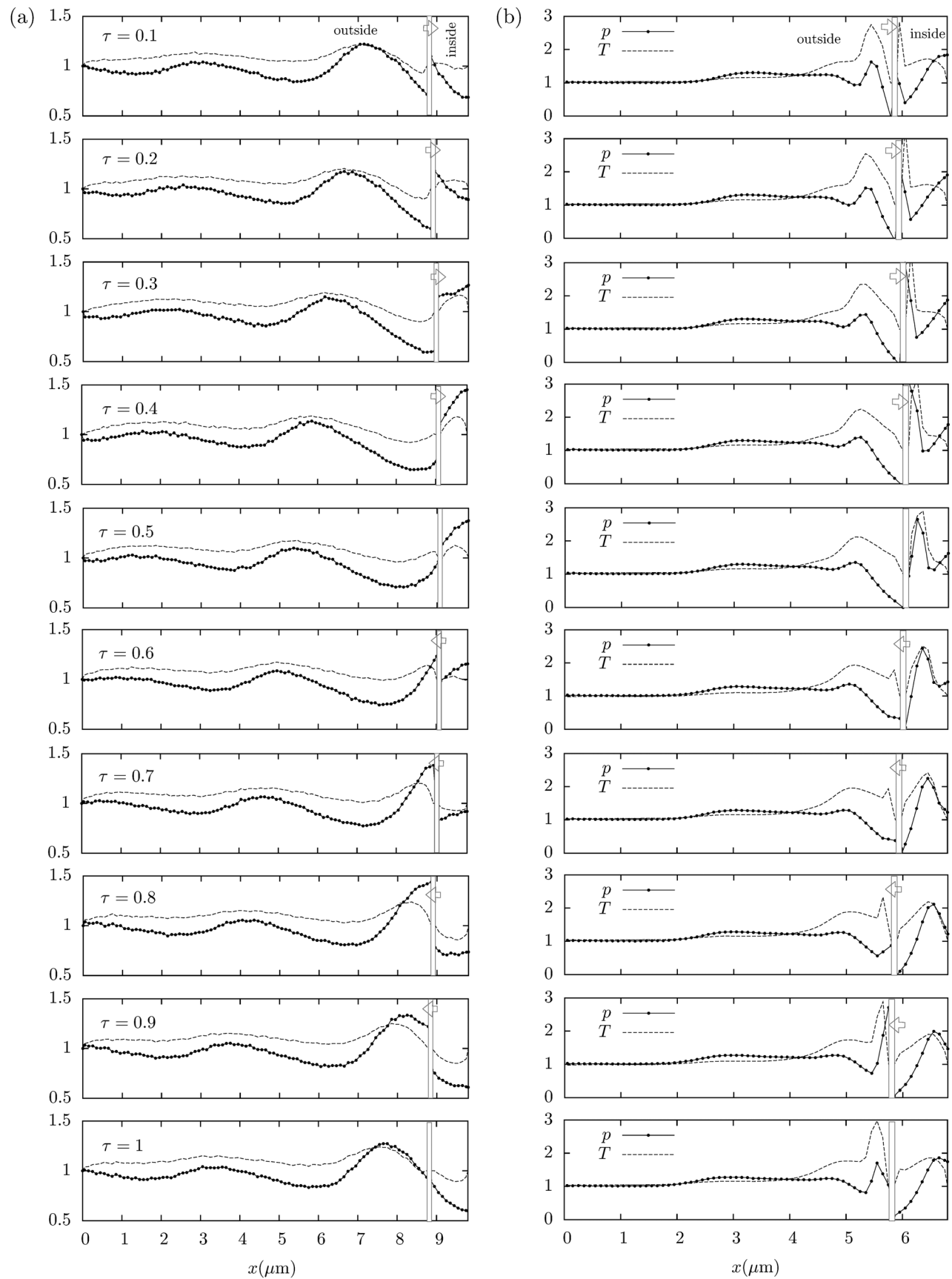


Fig. 9 Normalized pressure and temperature distributions along plane of symmetry during a period of beam oscillation. Left: case (a) and right: case (b).

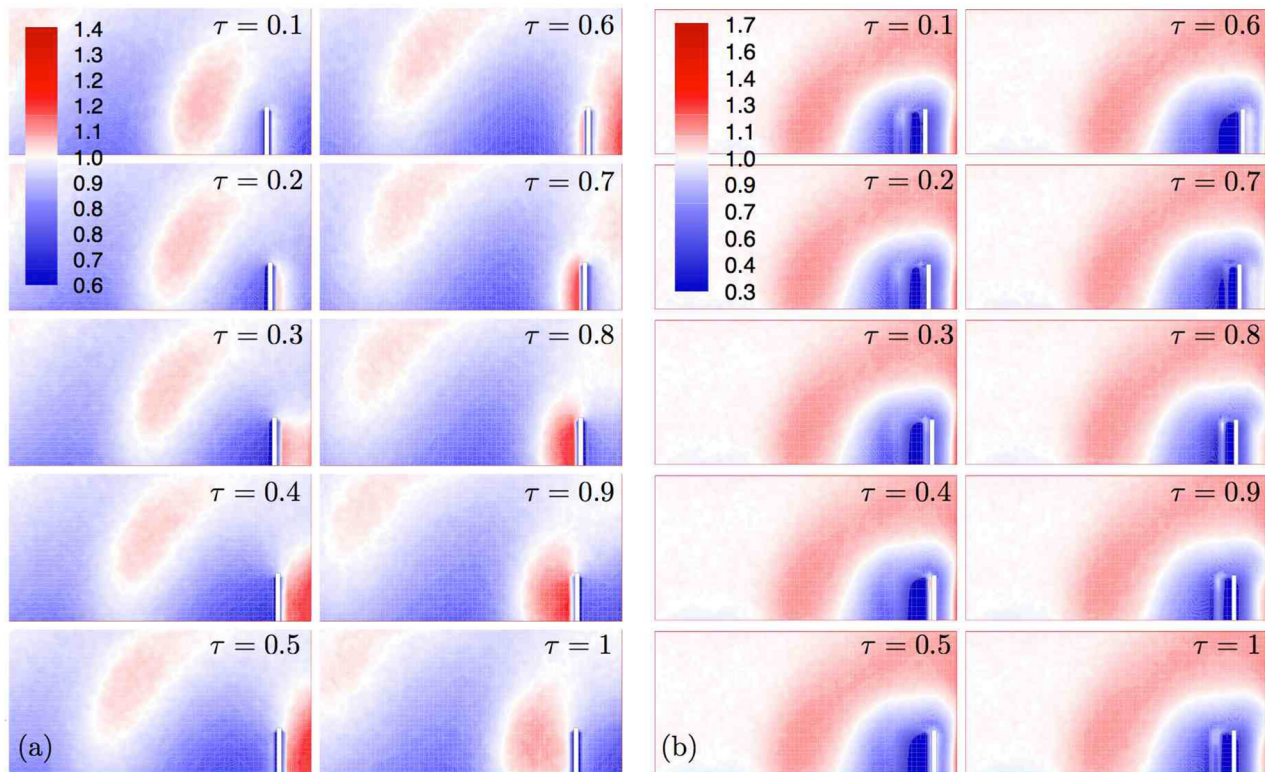


Fig. 10 Evolution of normalized density distribution over a period of beam oscillation. Left: case (a) and right: case (b).

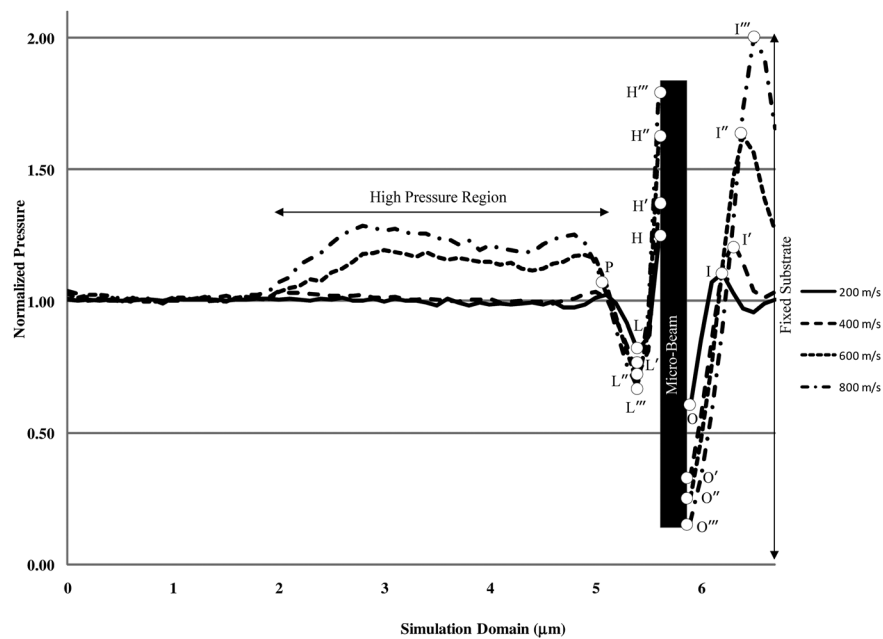


Fig. 11 Pressure distribution along plane of symmetry as a function of velocity amplitude V_a (set 1)

(points P_1'' , P_2'' , and P_3'' , respectively) and then decreases for $Ma^2 > 1.334$ (points P_4'' and P_5''). This transition is due to the interplay of compressibility effects of Ma and $Ma St$. While higher Ma introduces more compressibility as captured by larger peaks of pressure waves, higher $Ma St$ implies that the beam oscillation frequency gains a bigger role to the point where the beam inverts its oscillating direction so quickly that it reduces the amplitude of the pressure wave in its vicinity.

Figure 13 shows double cusps for the peak pressure variation over a whole period for the high oscillating frequencies. This is due to the effect of the fixed substrate where the pressure wave moving in front of the microbeam (due to inertia effects) meets the pressure wave reflected by the substrate causing a drop in the pressure peak amplitude.

According to Fig. 14, the speed of the pressure waves in the flow field approaches unity for large values of Ma , indicating that

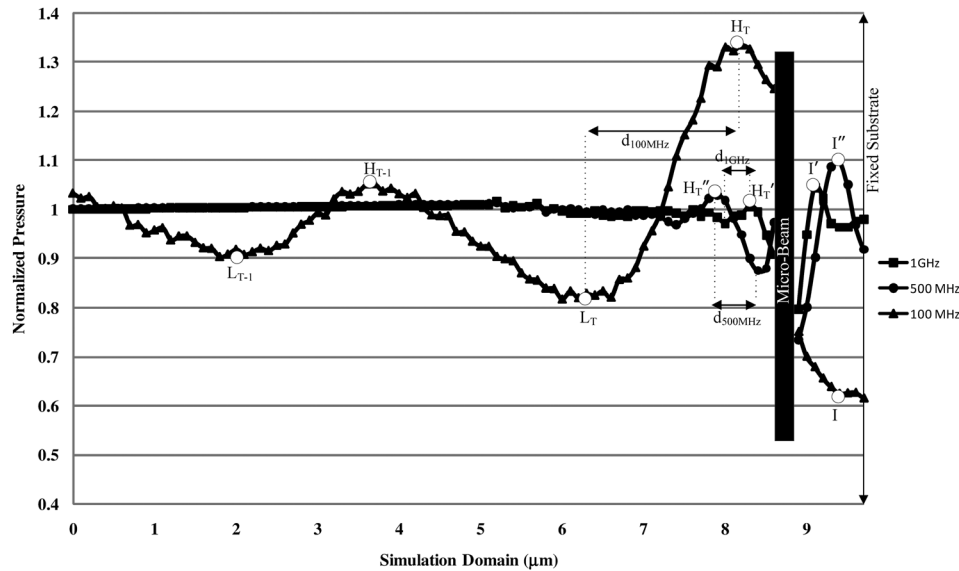


Fig. 12 Pressure distribution along plane of symmetry as a function of frequency f (set 2)

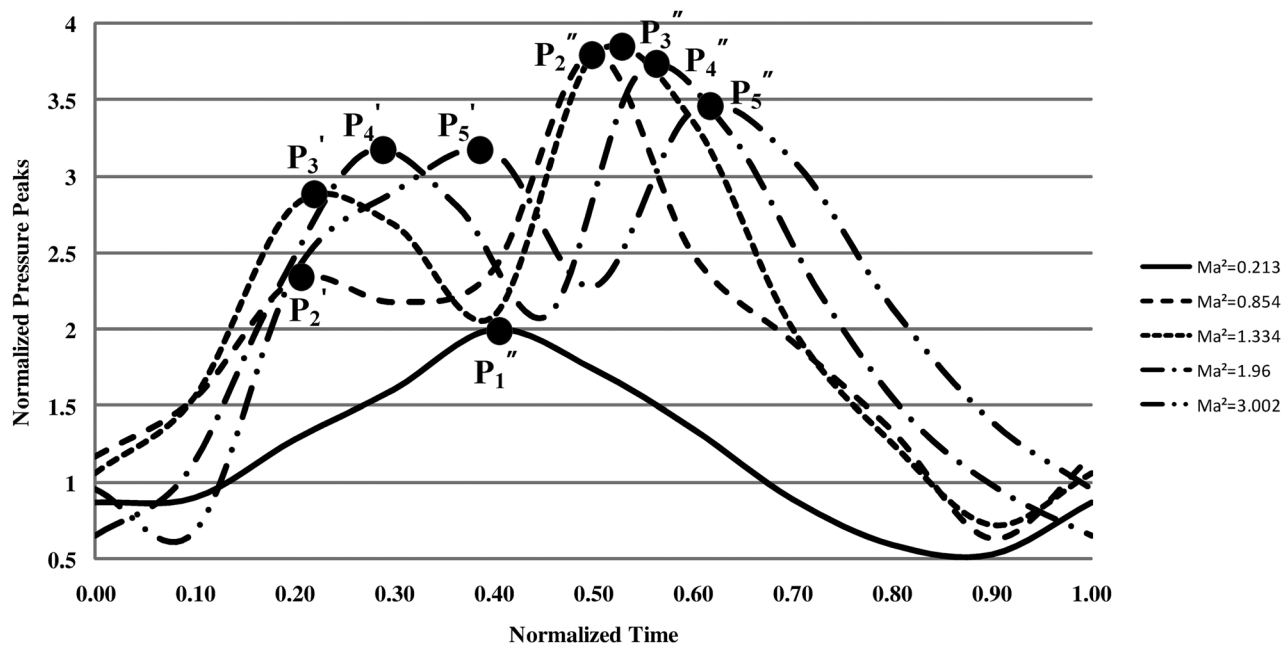


Fig. 13 Pressure waves peaks at the inside region as a function of Ma^2 over a complete period of motion (set 3)

the pressure waves acquire the speed of the beam when the speed of the beam exceeds that of sound (similar to case (b) of set 1). For values of $Ma^2 < 1$, the pressure waves travel at approximately the speed of sound, as can be deduced from Fig. 14 (similar to case (a) of set 2).

5 Three-Dimensional (3D) Microcantilever Beam

In this section, simulations are performed on an oscillating microcantilever beam of width smaller than its length (i.e., 3D) as compared to that of a two-dimensional (2D) microcantilever plate (width \gg larger). Unlike the 2D microbeam which is modeled (in DSMC) as one cell along its width, the 3D microbeam is open at its sides. Therefore, in DSMC, standard conditions of temperature and pressure are assigned at the simulation domain after moving away a sufficient distance from beam sides. Figure 15 shows a top

view of the 3D computational domain where the microbeam $efgh$ of finite width w is cut in half at the centerline bc due to symmetry while the side view is shown in Fig. 16. All the microbeam sides along with side ab are modeled as diffusive walls at room temperature, bc is modeled as a symmetry plane with specular reflections, and the enclosed region $adcc'a'a$ contains the reservoir cells that impose the ambient conditions of temperature and pressure away from the oscillating beam.

Table 4 summarizes the geometrical parameters used and the ambient gas medium physical conditions. Table 5 lists physical and dimensional parameters for the cases investigated. In this set of simulations, two cases are studied, where $(Ma^2, Ma^2 St^2)$ are $(5.33, 2.16)$ and $(21.32, 8.65)$ for cases 1 and 2, respectively, while St is kept constant at 0.64.

Figure 17 shows the maximum pressure over a complete oscillation period in the gas film squeezed between the beam and

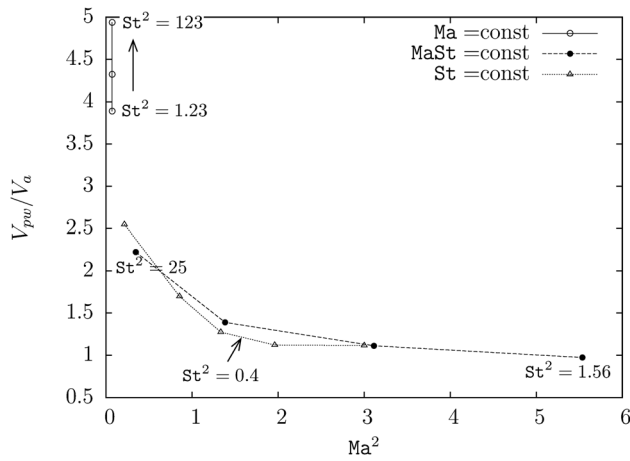


Fig. 14 Dependence of the normalized wave speed in the squeeze film region on Mach number

Table 4 Microbeam geometry and gas flow conditions

Physical property	Symbol	Value
Beam length	L	$5\ \mu\text{m}$
Beam thickness	t	$0.1\ \mu\text{m}$
Beam width ^a	w	$1\ \mu\text{m}$
Initial gap height	h_o	$1\ \mu\text{m}$
Ambient temperature	T_o	293 K
Ambient pressure (air)	P_o	101.1 KPa

^aOnly defined for the 3D beam.

Table 5 List of values for Ma^2 and Ma^2St^2 for the compressibility simulation case studies

		St	Ma ²	Ma ² St ²	Ma ² /Re
V _a (m/s)	f (MHz)	Set 1			
785	500	0.637	5.331	2.163	0.072
1570	1000	0.637	21.323	8.651	0.144

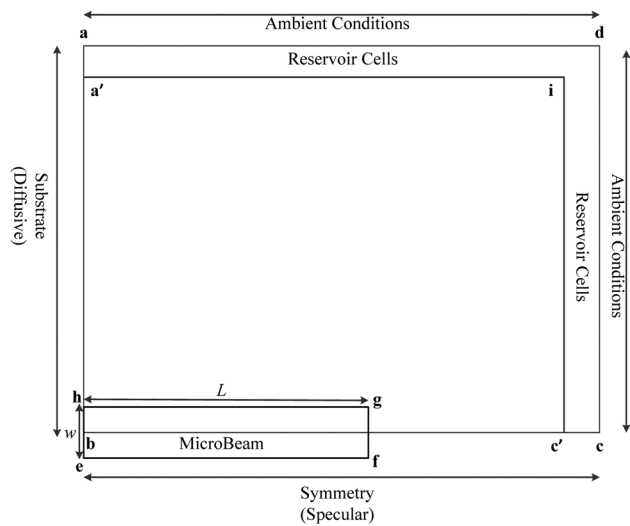


Fig. 15 Top view of the microbeam's 3D simulation domain

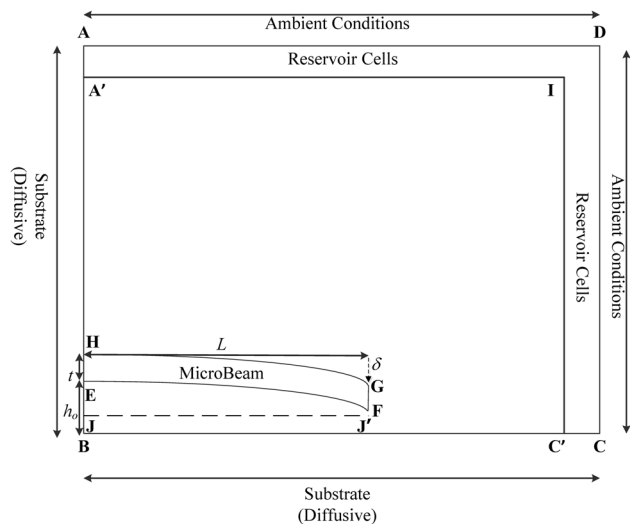


Fig. 16 Side view of the microbeam's 3D simulation domain

the substrate for both the 2D and 3D microbeams for case 1 in Table 5. It shows that at sufficiently high-beam oscillation frequencies (1 GHz), the pressure distributions underneath the 2D and 3D microbeams are similar indicating comparable compressibility effects whereas at lower frequencies (500 MHz), the pressure underneath the 2D beam is higher than that underneath the 3D microbeam indicating that the compressibility effects in the 2D case are larger than those in the 3D case. This behavior is explained by the fact that when the 3D beam is oscillating at a high frequency (i.e., 1 GHz), there is not enough time for the gas to flow between the squeeze film region underneath the microbeam and the surrounding medium. With the gas mostly “trapped” underneath the microbeam, its behavior underneath the 2D and 3D microbeams is similar. In such a case, the nonphysical boundaries extending from the beam peripheries ef and gh, as seen in Fig. 15, to the fixed substrate underneath approach the behavior of closed boundaries for both the 2D and 3D microbeams. However, at smaller oscillation frequencies (i.e., 500 MHz), there is more time for the gas to flow between the squeeze film region and its surrounding in the 3D case. In this case, compressibility effects are stronger in the squeeze film underneath the 2D microbeam since the gas can only escape under the fg side the beam, whereas for the 3D case, it can escape under the ef, fg, and gh sides.

The degree of compressibility can be assessed by comparing the time scale characterizing the gas flow between the squeeze film region and its surrounding to the period of oscillation of the beam. This is clearly reflected by the larger values of Ma^2 and Ma^2St^2 for the 1 GHz case as compared to the 500 MHz case implying that the compressibility effect for the former case is higher than that for the latter which agrees with the 2D compressibility analysis discussed in Sec. 4.3.

Mass flow rates of gas leaving and entering the squeeze region, as the beam travels toward and away from the substrate, are expected to be larger in the 3D case when compared to the 2D case, thus reducing the pressure in the squeeze film underneath the 3D beam when its oscillation frequency is sufficiently low, as depicted in Fig. 17. The computed gas average mass flow rate underneath the 3D microbeam's boundaries for the 1 GHz at the time where pressure in the squeeze film is largest (i.e., at $\tau_{\text{norm}} = 0.3$ in Fig. 15) is 3.8727×10^{-12} kg/s, whereas the corresponding value for the 500 MHz case is 1.0056×10^{-13} kg/s, which is in agreement that higher pressure in the squeeze film is associated with smaller gas mass flow rates. Moreover, the average mass flow rate underneath the microbeam sides (i.e., ef and gh in Fig. 15) is larger in the 500 MHz case (1.0474×10^{-12} kg/s) than that in the 1 GHz (1.3171×10^{-13} kg/s) due to the fact that

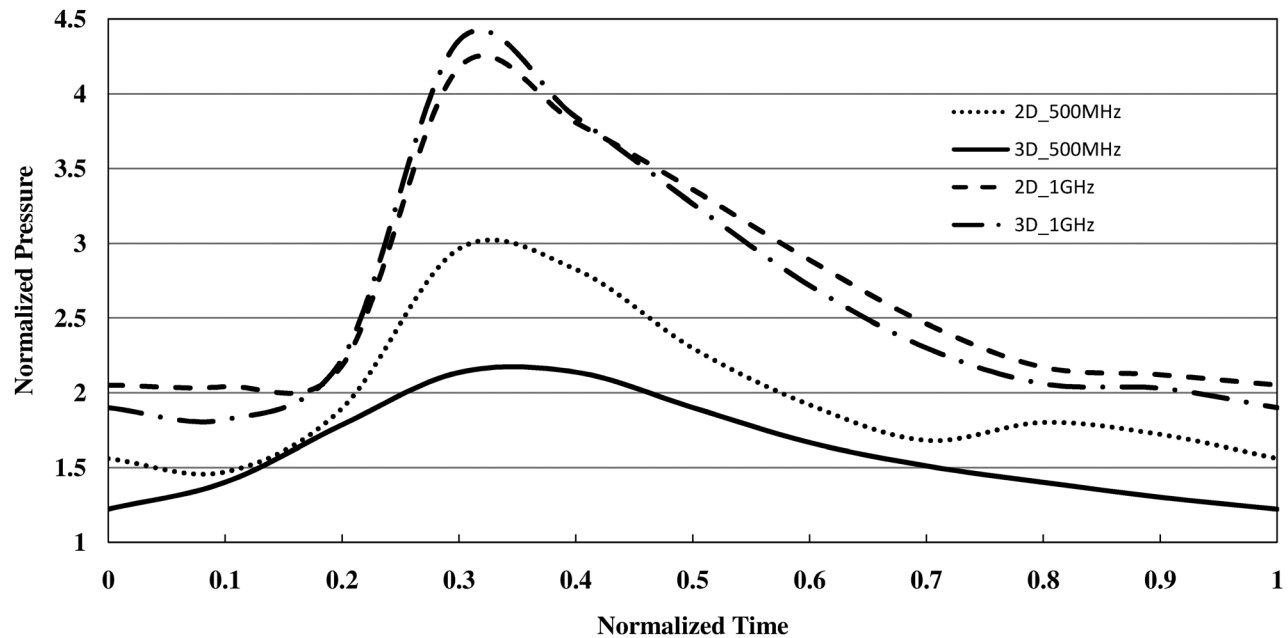


Fig. 17 Pressure peaks for the 2D and 3D microcantilever beams oscillating at 500 MHz and 1 GHz

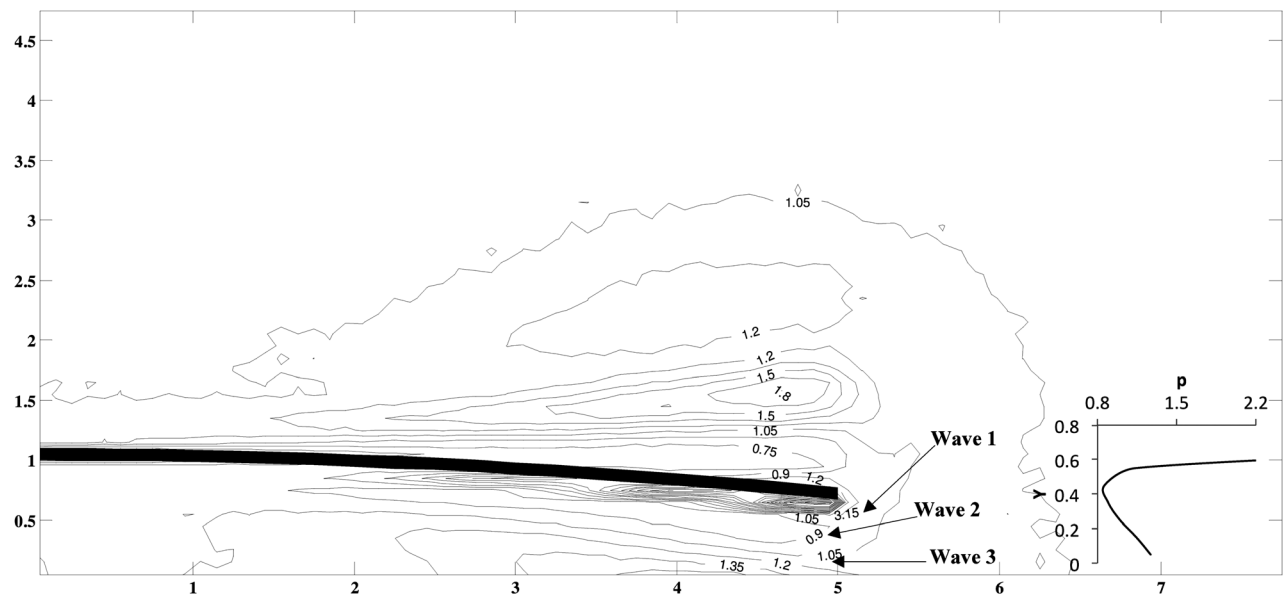


Fig. 18 Pressure contours in the cross-sectional plane of the 3D microcantilever beam oscillating at 1 GHz. Pressure variation at $x = 5$ from ground to beam tip is shown in the inset.

the squeezed air has more time to spread throughout the film gap and consequently to its surroundings. However, by precisely looking at the mass flow rate underneath the beam tip (i.e., fg in Fig. 15) alone, the average mass flow rate for the 1 GHz microbeam was found to be 2.943×10^{-12} kg/s which is larger than that of the 500 MHz calculated as 5.8786×10^{-13} kg/s, which appears to be contradicting to the gas “entrapment” phenomena discussed earlier. To further investigate this apparent contradiction, we focus on the dynamics of the gas flow in the region of the beam tip (fg). Figure 18 (x and y axes represent the simulation domain in μm) shows the pressure contours at the time where the microbeam is moving toward the fixed substrate at its maximum speed (i.e., $\tau_{\text{norm}} = 0.3$). It can be seen from the figure there exist two high pressure (waves 1 and 3) and one low-pressure wave (wave 2) during the compression first half period, the first

high-pressure wave is from the current period and the second high-pressure wave along with the low-pressure wave is from the previous period. Note that this figure along with all the figures that follow for the 3D beam represents a cross-sectional view of the symmetry plane (represented by bc in Fig. 15) cutting the 3D microcantilever beam in half.

The corresponding gas flow velocity field, presented in Fig. 19, shows that in region B underneath the microbeam tip, the gas flows from inside the squeeze film to the outside due to the high-pressure wave (wave 3 in Fig. 18) that persisted from the first half period of the previous oscillation cycle which is “not trapped” anymore and had enough time to induce mass flow outside the gap region.

Figure 20 shows a different flow behavior beneath the beam tip when the oscillation frequency is 500 MHz. In this case, two

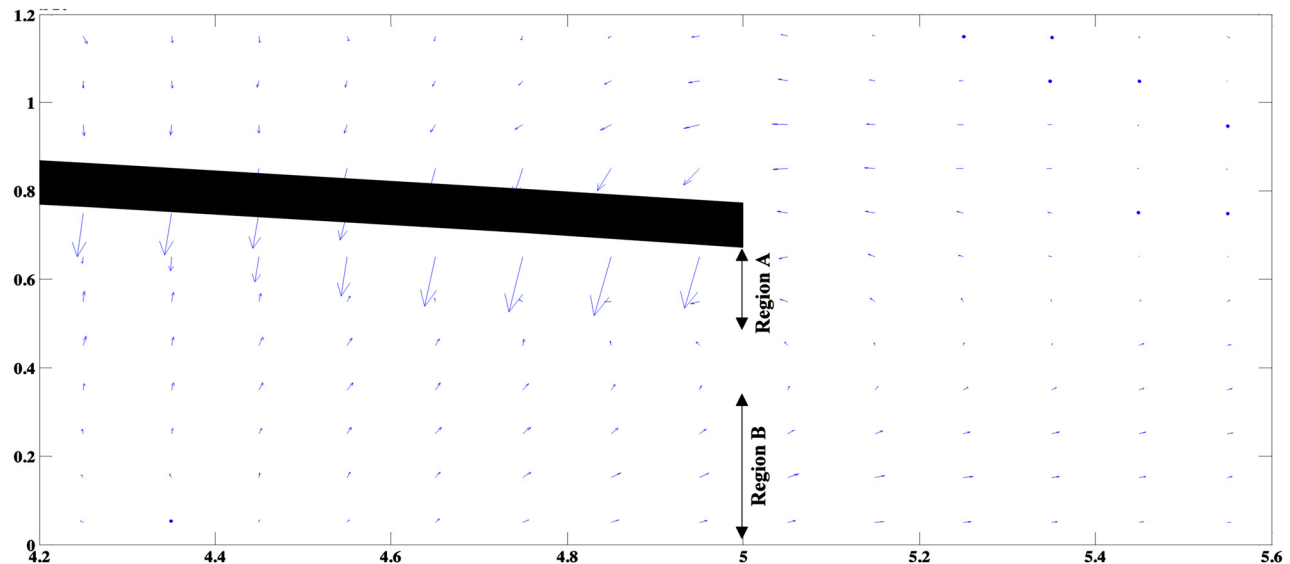


Fig. 19 Velocity flow field for the cross-sectional plane of the 3D microcantilever beam oscillating at 1 GHz

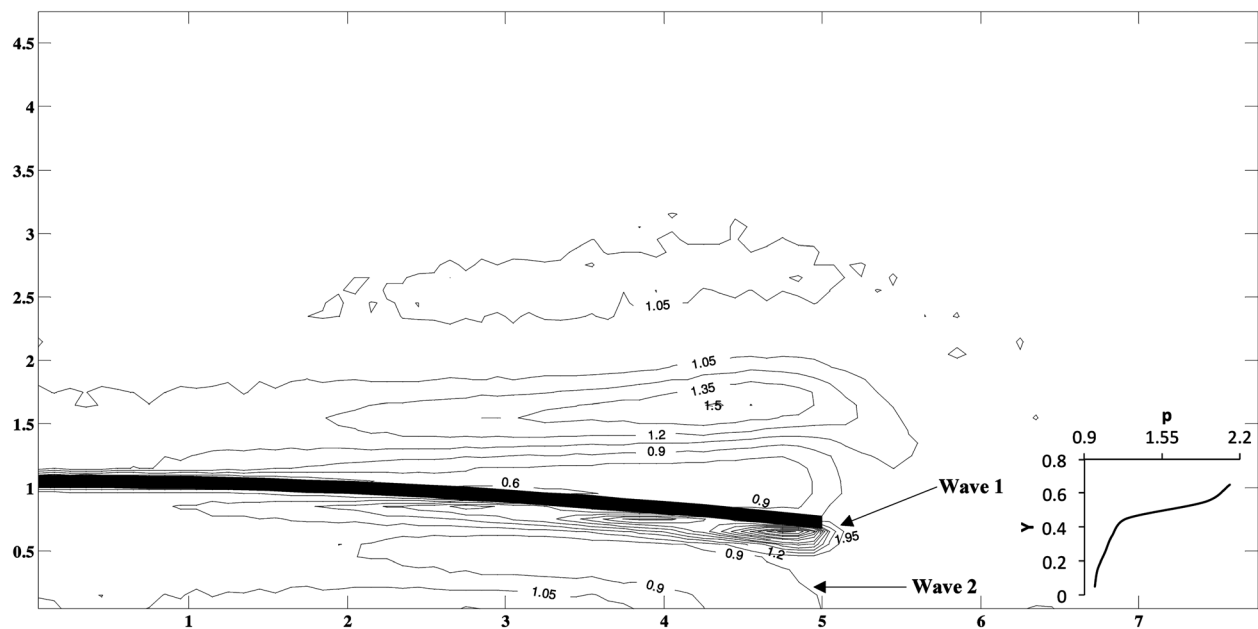


Fig. 20 Pressure contours in the cross-sectional plane of the 3D microcantilever beam oscillating at 500 MHz. Pressure variation at $x = 5$ from ground to beam tip is shown in the inset.

pressure waves are present beneath the beam tip: a high-pressure wave (wave 1) and a low-pressure wave (wave 2). The absence of the third high-pressure wave (that was observed in the 1 GHz case) is explained as follows. By the time the beam starts a new oscillation cycle, the intensity of the high-pressure wave caused by the previous cycle has faded away and in this case the high-pressure wave formed by the current period coexists only with the low-pressure wave caused by the second half period of the previous oscillatory cycle (i.e., destructive effect). This behavior creates the coexisting high (wave 1) and low (wave 2) pressure gap regions underneath the oscillating microbeam as seen in Fig. 20 which tends to locally decrease the mass flow rate at the microbeam's tip as compared to the 1 GHz case with the high-pressure gap region. This is confirmed by inspecting the gas flow velocity field near the beam tip presented in Fig. 21 where it can be seen that in region B, the gas flows from outside to the inside of the

squeeze region due to the presence of the low-pressure wave (wave 2 in Fig. 20) from the second half period of the previous cycle.

Therefore, the coexistence of the second high-pressure wave (wave 3 in Fig. 18) for the 1 GHz case induces a mass flow rate escaping the squeeze region at the microbeam's tip that is larger than that of the 500 MHz case where such a high-pressure wave does not coexist with the newly formed high-pressure wave.

The existence of these high-pressure waves underneath the microbeam's tip tends to increase the pressure at the back face of both the 2D and 3D microbeams due to flow circulation around the microbeam's tip. This can be observed from Fig. 22, where the force acting on the microbeam's back face is plotted versus the beam's length, for both the 500 MHz and 1 GHz cases at $\tau_{\text{norm}} = 0.3$. For both cases, the force starts with a value close to that exerted by atmospheric pressure at the microbeam's fixed end

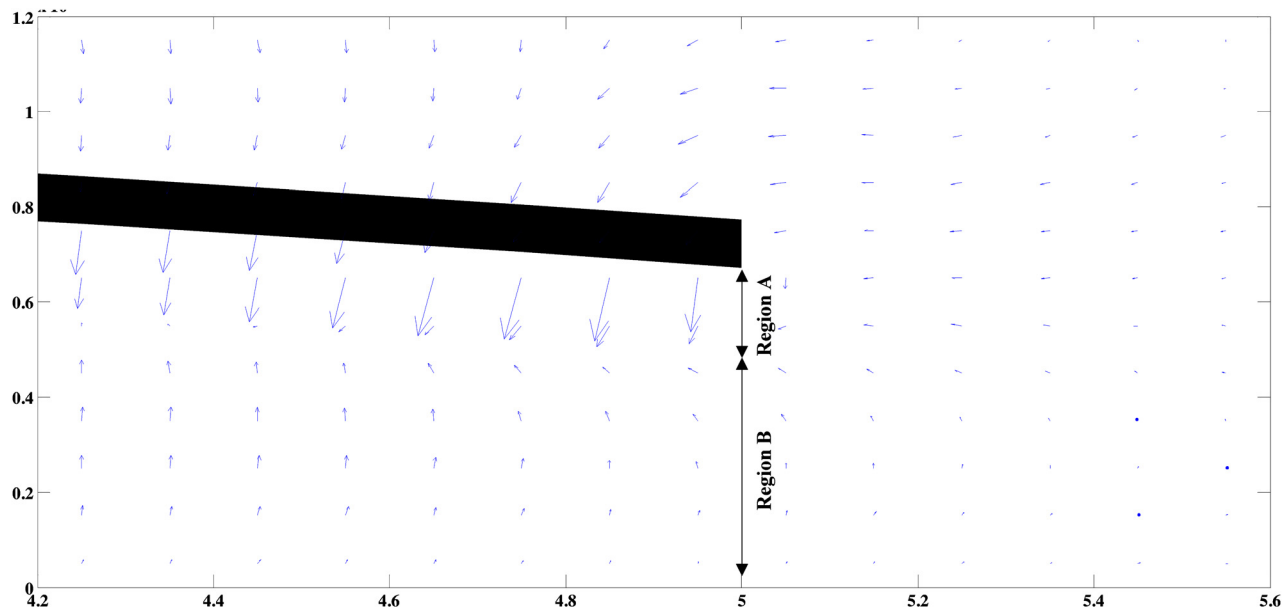


Fig. 21 Velocity flow field for the cross-sectional plane of the 3D microcantilever beam oscillating at 500 MHz

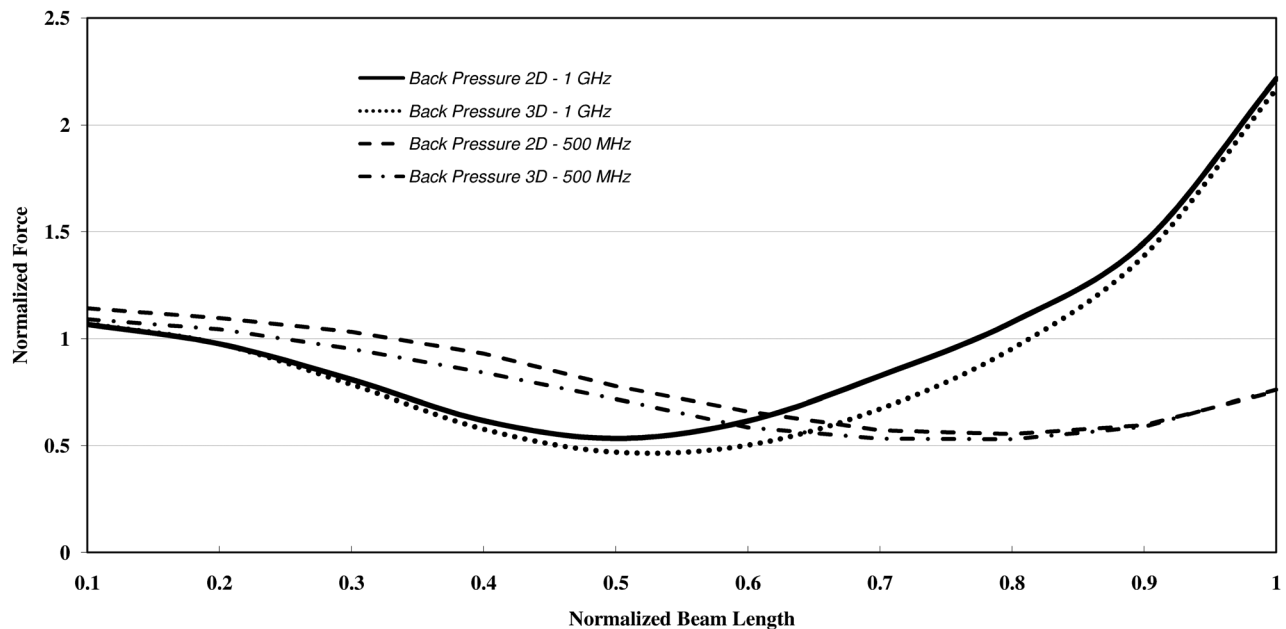


Fig. 22 Force distribution at the back beam face for the 2D and 3D microcantilever beams oscillating at 500 MHz and 1 GHz

and then starts decreasing as expected since the microbeam is moving toward the fixed substrate thus creating a low-pressure region at its back face. However, as we move closer to the microbeam's tip, the back beam force experiences an increase due to circulation induced by the high-pressure, high-density, and high-speed gas flow escaping just underneath the tip. This increase is much more intense for the 1 GHz case due to the higher mass flow rate underneath the tip, as already demonstrated.

6 Conclusion

The dynamic force on a microbeam oscillating above a substrate imparted by a surrounding medium is investigated for a range of oscillating speed amplitudes and frequencies. The micro-flow behavior of the gas film between the beam and the substrate and its relation to the forces acting on the front and back sides of the beam are interpreted in terms of the relative contributions of

diffusion and the unsteady and convective components of inertia, as quantified by the various dimensionless groups. It has been observed that for larger values of Reynolds number (i.e., inertia effects), the force on the side of the beam facing the substrate (front face) departs from the harmonic profile of the beam motion and the force amplitude on both beam faces during the second half period is larger than their counterparts during the first half period. For small Strouhal number, the phase difference between the beam and flow within the gap decreases. When Re and St are small, diffusion plays a dominant role over inertia, increasing the phase difference between the beam's motion and front face force and decreasing the front face force amplitude. This corresponds to relatively low squeeze number where the gas has enough time to diffuse and escape from getting trapped between the oscillating beam and the fixed substrate. The compressible effects of the gas are shown to be dependent on the values of Ma^2 and $Ma^2 St^2$. It has been observed that when the beam oscillates at a low Ma , the

pressure waves travel at a near sonic speed, while for high Ma the pressure wave speed approaches the speed of the beam itself. Finally, a 3D microbeam was simulated and the behavior of the pressure waves in its vicinity was compared to those of a 2D microbeam under the same conditions. The force distribution at the microbeam's faces was plotted, and the effect of circulation around the beam's tip was clearly indicated which plays a significant role in designing micro-RF switches especially at the point of contact (i.e., tip).

Nomenclature

b = microplate width
 c = damping constant
 f = oscillation frequency
 F_{net} = net force
 h_0 = initial gap film thickness
 Kn = Knudsen number
 L = microplate length
 Ma = Mach number
 p_a = ambient pressure
 p_b = microplate's back face pressure
 p_f = microplate's front face pressure
 Re = Reynolds number
 St = Strouhal number
 t = microplate thickness
 V_a = microplate velocity amplitude
 ω_c = cutoff frequency
 δ = oscillation amplitude
 μ = dynamic viscosity
 ρ = gas density
 σ_L, σ_b = squeeze numbers

References

- [1] Muller, P., Rolland, N., Ziaei, A., Polizzi, J., Collard, D., and Buchailot, L., 2005, "Bulk Microswitch for Power RF Applications," 18th *IEEE International Conference on Micro Electro Mechanical Systems, MEMS*, Jan. 30–Feb. 3, pp. 171–174.
- [2] Pryputniwicz, R., Xiangguang, T., and Przekwas, A., 2004, "Modeling and Measurements of MEMS Gyroscopes," *IEEE Position Location and Navigation Symposium*, pp. 111–119.
- [3] Juan, W., and Pang, S., 1998, "High-Aspect-Ratio Si Vertical Micromirror Arrays for Optical Switching," *J. Microelectromech. Syst.*, **7**(2), pp. 207–213.
- [4] Beliveau, A., Spencer, G., Thomas, K., and Roberson, S., 1999, "Evaluation of MEMS Capacitive Accelerometers," *IEEE Des. Test Comput.*, **16**(4), pp. 48–56.
- [5] Yasseen, A., Wu, C., Zorman, C., and Mehregany, M., 2000, "Fabrication and Testing of Surface Micromachined Polycrystalline SiC Micromotors," *IEEE Electron Device Lett.*, **21**(4), pp. 164–166.
- [6] Mehra, A., Zhang, X., Ayn, A., Waitz, I., Schmidt, M., and Spadaccini, C., 2000, "A Six-Wafer Combustion System for a Silicon Micro Gas Turbine Engine," *J. Microelectromech. Syst.*, **9**(4), pp. 517–527.
- [7] Blech, J., 1983, "On Isothermal Squeeze Films," *J. Lubr. Technol.*, **105**(4), pp. 615–620.
- [8] Andrews, M., Harm, I., and Turner, G., 1993, "A Comparison of Squeeze-Film Theory With Measurements on a Microstructure," *Sens. Actuators A*, **36**(1), pp. 79–87.
- [9] Zook, J., Bums, D., Guckel, H., Sniegowski, J., Engelstad, R., and Feng, Z., 1992, "Characteristics of Polysilicon Resonant Microbeams," *Sens. Actuators A*, **35**(1), pp. 51–59.
- [10] Guo, X., and Alexenko, A., 2009, "Compact Model of Squeeze-Film Damping Based on Rarefied Flow Simulations," *J. Micromech. Microeng.*, **19**(4), p. 045026.
- [11] Bao, M., Yang, H., Yin, H., and Sun, Y., 2002, "Energy Transfer Model for Squeeze-Film Air Damping in Low Vacuum," *J. Micromech. Microeng.*, **12**(3), pp. 341–346.
- [12] Christian, R., 1966, "The Theory of Oscillating-Vane Vacuum Gauges," *Vacuum*, **16**(4), pp. 175–178.
- [13] Newell, W., 1968, "Miniaturization of Tuning Forks," *Science*, **161**(3848), pp. 1320–1326.
- [14] Hutcherson, S., and Ye, W., 2004, "On the Squeeze-Film Damping of Micro-Resonators in the Free-Molecule Regime," *J. Micromech. Microeng.*, **14**(12), pp. 1726–1733.
- [15] Li, P., and Fang, Y., 2010, "A Molecular Dynamics Simulation Approach for the Squeeze-Film Damping of MEMS Devices in the Free Molecular Regime," *J. Micromech. Microeng.*, **20**(3), p. 035005.
- [16] Bao, M., Sun, Y., Zhou, J., and Huang, Y., 2006, "Squeeze-Film Air Damping of a Torsion Mirror at a Finite Tilting Angle," *J. Micromech. Microeng.*, **16**(11), pp. 2330–2335.
- [17] Langlois, W. E., 1962, "Isothermal Squeeze Films," *Q. Appl. Math.*, **20**, pp. 131–150.
- [18] Starr, J. B., 1990, "Squeeze-Film Damping in Solid-State Accelerometers," Technical Digest *IEEE Solid State Sensor and Actuator Workshop*, Hilton Head Island, SC, June 4–7, pp. 44–47.
- [19] Veijola, T., Tinttunen, T., Nieminen, H., Ermolov, V., and Ryhnen, T., 2002, "Gas Damping Model for a RF MEM Switch and Its Dynamic Characteristics," International Microwave Symposium (IMS), Seattle, WA, June 2–7, pp. 1213–1216.
- [20] Veijola, T., 2004, "Compact Models for Squeezed-Film Dampers With Inertial and Rarefied Gas Effects," *J. Micromech. Microeng.*, **14**(7), pp. 1109–1118.
- [21] Gallis, M., and Torczynski, J., 2004, "An Improved Reynolds-Equation Model for Gas Damping of Microbeam Motion," *J. Microelectromech. Syst.*, **13**(4), pp. 653–659.
- [22] Lee, J., Tung, R., Raman, A., Sumali, H., and Sullivan, J., 2009, "Squeeze-Film Damping of Flexible Microcantilevers at Low Ambient Pressures: Theory and Experiment," *J. Micromech. Microeng.*, **19**(10), p. 105029.
- [23] Sumali, H., 2007, "Squeeze-Film Damping in the Free Molecular Regime: Model Validation and Measurement on a MEMS," *J. Micromech. Microeng.*, **17**(11), pp. 2231–2240.
- [24] Mol, L., Rocha, L., Cretu, E., and Wolffenbuttel, R., 2009, "Squeezed Film Damping Measurements on a Parallel-Plate MEMS in the Free Molecule Regime," *J. Micromech. Microeng.*, **19**, p. 074021.
- [25] Diab, N., and Lakkis, I., 2014, "Modeling Squeezed Films in the Vicinity of High Inertia Oscillating Micro-Structures," *ASME J. Tribol.*, **136**(2), p. 021705.
- [26] Diab, N., and Lakkis, I., 2012, "DSMC Simulations of Squeeze Film Between a Micro Beam Undergoing Large Amplitude Oscillations and a Substrate," *ASME Paper No. ICNMM2012-73138*.
- [27] Bird, G. A., 1994, *Molecular Gas Dynamics and the Direct Simulation of Gas Flows*, Clarendon, Oxford, UK.
- [28] Karniadakis, G., Beskok, A., and Aluru, N., 2005, *Microflows and Nanoflows*, Springer-Verlag, New York.
- [29] Shen, C., 2005, *Rarefied Gas Dynamics*, Springer, Berlin.
- [30] Veijola, T., Kuisma, H., Lahdenpera, J., and Ryhanen, T., 1995, "Equivalent-Circuit Model of the Squeezed Gas Film in a Silicon Accelerometer," *Sens. Actuators A*, **48**(3), pp. 239–248.
- [31] Batchelor, G., 2000, *An Introduction to Fluid Dynamics*, Cambridge University Press, Cambridge, UK.